Journal of Computational Physics 550 (2026) 114653

Contents lists available at ScienceDirect

Journal of Computational Physics

journal homepage: www.elsevier.com/locate/jcp

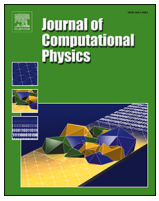

A Central Differential flux with high-Order dissipation for robust simulations of transcritical flows ⋆

Bonan Xu [a], Chang Sun [b], Peixu Guo [a,*]

[a] Department of Aeronautical and Aviation Engineering, The Hong Kong Polytechnic University, 11 Yuk Choi Road, Hong Kong SAR, China
[b] Department of International Cooperation, BeijingMicroelectronics Technology Institute, No.2, North Siyingmen Road, 100076, Beijing, China

ARTICLE INFO

Keywords:
Transcritical flow
Primitive-variable formulation
Hybrid scheme
Pressure oscillations

ABSTRACT

The simulation of transcritical flows remains challenging due to strong thermodynamic nonlinearities that induce spurious pressure oscillations in conventional schemes.While primitive-variable formulations offer improved robustness under such conditions, they are always limited by energy conservation errors and the absence of systematic high-order treatments for numerical fluxes. In this paper, we introduce the Central Differential flux with High-Order Dissipation (CDHD), a novel numerical flux solver designed for primitive-variable discretization. This method combines a central flux for advection with a minimal, upwind-biased dissipation term to stabilize the simulation while maintaining formal accuracy. The dissipation term effectively suppresses oscillations and improves stability in transcritical flows. Compared to traditional primitive-variable approaches, CDHD reduces the energy conservation error in two order of magnitude. When incorporated into a hybrid framework with a conservative shock-capturing scheme, the method robustly handles both smooth transcritical phenomena and shock waves. Numerical tests validate the accuracy, stability, and energy-preserving capabilities of CDHD, demonstrating its potential as a reliable tool for complex real-gas flow simulations.

1. Introduction

The accurate simulation of fluids in the transcritical regime is essential for the design and analysis of advanced engineering systems[1], such as liquid rocket engines [2–5], supercritical power cycles [6–8], and next-generation chip cooling systems [9,10]. As shown in Fig. 1, the regime located near the pseudo-boiling or Widom line[11,12], is characterized by drastic, liquid-like to gas-like variations in thermodynamic and transport properties. These strong thermodynamic nonlinearities introduce new fluid phenomena [13–16] but present significant challenges for numerical simulations [17]. The application of widely used conservative schemes often generates severe unphysical pressure oscillations [18] that can render the simulation unstable. Even in ideal gas flows, similar oscillations can be observed in regions with rapid property change, such as material interfaces[19] or in multicomponent flows [20–22]. Thus, accurately capturing these transcritical phenomena requires not only a precise real-gas Equation of State (EoS), such as the Peng-Robinson [23,24] model utilized in this paper, but also a numerical scheme that is both accurate and robust.

To address these numerical challenges, numerous attempts have been made to suppress these unphysical oscillations. For low-velocity transcritical flows, researchers have widely adopted the low-Mach-number approximation [25–27] of the governing equations. For instance, Pasquale [28] use a low-Mach approximation in the direct numerical simulation to fully resolve the interaction

⋆ This research is supported by theStart-up Fund for RAPs by the Hong Kong Polytechnic University.
* Corresponding author.
E-mail address: peixu.guo@polyu.edu.hk, peixu.guo@outlook.com (P. Guo).

https://doi.org/10.1016/j.jcp.2026.114653
Received 31 August 2025; Received in revised form 23 December 2025; Accepted 2 January 2026
Available online 7 January 2026

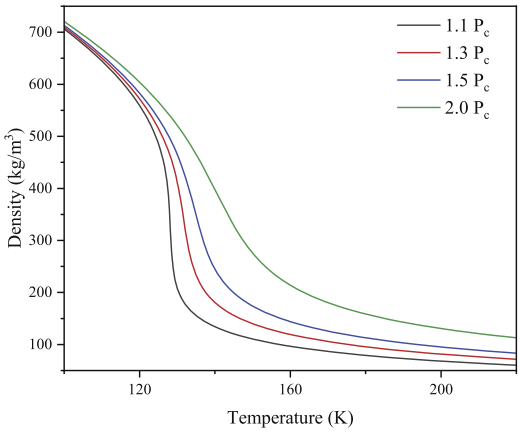

(a) Density

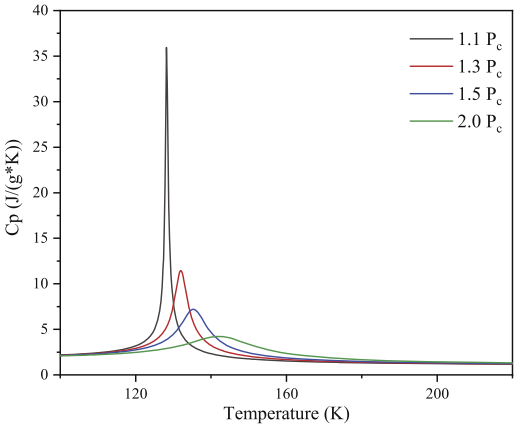

(b) Constant pressure specific heat capacity

Fig. 1. Density and constant pressure specific heat capacity of transcritical nitrogen at different pressures. The critical pressure P_c of nitrogen is 3.3958MPa and the critical temperature T_c is 126.192K.

between turbulent and transcritical layers in a nitrogen jet. While effective and robust for low-velocity flows, this approximation can introduce non-negligible errors when the flow Mach number exceeds 0.1. Thus, many new numerical methods have been developed based on non-conservative formulations. The double flux method [29] that is originally designed to reduce the pressure oscillation in multicomponent flows is used for the simulation of transcritical flows [18,30–32]. Instead of using the total energy equation, the pressure evolution equation [33–36] is extensively employed for transcritical flow simulation. Kawai et al. successfully employ a high-order compact differencing scheme to solve the pressure evolution equation for a robust and accurate simulation of transcritical flows [36]. However, these non-conservative methods, including the double-flux and pressure evolution formulations, come at the cost of energy conservation error, which can lead to an incorrect prediction of shock wave locations and strengths. To reduce this conservation error, hybrid methods [22,37–39] are also developed by researchers. Bradley Boyd and Dorrin Jarrahbashi [39] propose a hybrid scheme that switches between a double-flux in transcritical region and a traditional fully conservative method for other simulation domains. An emerging research topic in recent years is the development of fully conservative schemes to effectively suppress pressure oscillations during real-fluid simulations [40]. Eric Ching et at. develop a fully conservative discontinuous Galerkin method for supercritical, real-fluid flows [41] that uses an L^2 projection of primitive variables [42–44] to reduce pressure oscillations. While this approach maintains stability, it can still result in small deviations from pressure equilibrium. More recently, Fujiwara et al. derive a pressure-equilibrium condition [45] from the governing equations and constructed numerical fluxes to implicitly maintain this condition. Terashima et al. extend this method to real fluids [46], proposing an approximately pressure-equilibrium-preserving scheme with full energy conservation. However, these methods [45–47] are not easily extended to general transcritical flows.

Despite these advances, the pressure evolution equation remains a promising approach for the robust simulation of transcritical flows. An open source code called CUBENS [48] is recently developed based on the pressure evolution equation for the simulation of real fluid including transcritical flows. However, several key challenges persist. Firstly, discretizing the pressure evolution equation can lead to an incorrect prediction of shock wave locations and strength. Secondly, the energy conservation error should be minimized

for industrial applications where heat transfer is critical. Finally, a robust, high-order, and easily extendable numerical flux solver for the primitive variable form of the equation has yet to be developed.

This paper presents a hybrid numerical method designed to address these challenges. We utilize a hybrid framework that switches between a non-conservative, primitive-variable update in smooth regions and a fully conservative update in shock regions. The Primitive Variable Riemann Solver (PVRS) [49] is utilized as a sensor to dynamically switch to a fully conservative scheme (fifth-order WENO [50] with Roe flux [51]) to ensure accurate and robust shock capturing. For the primitive-variable update, we propose a new interface flux solver called Central Differential flux with High-order Dissipation (CDHD) for the pressure evolution equation. This method uses a high-order central flux to provide accuracy for the convection term and augments it with a small, high-order, upwind-biased dissipation term to provide the necessary stabilization for transcritical gradients without degrading the formal order of accuracy. A rigorous error analysis shows that the overall order of accuracy is determined by the central flux, provided that the dissipation term is computed using high-order reconstructed values. Due to its low numerical diffusion, the proposed scheme demonstrates superior energy conservation in smooth regions compared to conventional primitive-variable methods. The hybrid framework ensures robustness for a wide range of flows containing both smooth transcritical phenomena and shocks.

The remainder of this paper is organized as follows: In Section 2, the mathematical model, including the governing equations and thermodynamic closure, is described. In Section 3, we detail the components of the hybrid numerical method. Section 4 provides a formal error analysis justifying the accuracy of the proposed scheme. In Section 5, we present validation results from several one-dimensional (1D) and two-dimensional (2D) test cases to demonstrate the accuracy, stability, and robustness of the proposed scheme. Finally, Section 6 summarizes of the findings.

2. Mathematical model

2.1. Governing equations

The governing equations for inviscid transcritical fluid flows are the Euler equations. For clarity, the numerical method is derived and presented for the 1D case. The extension of the proposed method to multiple dimensions is straightforward, as will be demonstrated later with a two-dimensional test case.

The one-dimensional Euler equations can be expressed in a standard conservative form:

$$\frac{\partial \mathbf{W}}{\partial t} + \frac{\partial \mathbf{F}(\mathbf{W})}{\partial x} = 0, \tag{1}$$

where $\mathbf{W} = [\rho, \rho u, E]^T$ represents the vector of conservative variables (ρ for density, u for velocity, E for total energy), and $\mathbf{F}(\mathbf{W}) = [\rho u, \rho u^2 + p, u(E + p)]^T$ is the flux. The pressure p is obtained from a real-gas EoS. Alternatively, in quasi-linear primitive form using $\mathbf{V} = [\rho, u, p]^T$, the equations become

$$\frac{\partial \mathbf{V}}{\partial t} + B(\mathbf{V})\frac{\partial \mathbf{V}}{\partial x} = 0, \tag{2}$$

where

$$B(\mathbf{V}) = \begin{bmatrix} u & \rho & 0 \\ 0 & u & 1/\rho \\ 0 & \rho c^2 & u \end{bmatrix}, \tag{3}$$

and c is the speed of sound, computed via the corresponding EoS of the working fluid.

2.2. Thermodynamic closure and equation of state

An accurate description of the thermodynamic nonlinearity for fluids in the transcritical regime is of primary significance. The extreme variations in fluid properties, particularly near the pseudo-boiling or Widom line, require that a thermodynamic model can accurately capture these strong nonlinearities. While the numerical method in this work is developed to be general and compatible with any sufficiently complex EoS, all computations herein will utilize the Peng-Robinson (PR) EoS [23,24]. The PR-EoS is a cubic EoS that has been shown to reliably predict the thermodynamic properties [52] for hydrocarbons and other fluids in transcritical and supercritical regions. Thus, the PR-EoS should be a suitable choice for the simulation of transcritical fluids.

To be specific, the PR EoS is expressed as

$$P = \frac{\rho R_u T}{M_w - b\rho} + \frac{a\alpha(T)\rho^2}{M_w^2 + 2M_w b\rho - b^2\rho^2}, \tag{4}$$

where R_u is the universal gas constant, M_w is the molar mass, and T is the absolute temperature.

In this work we use the original Peng-Robinson form for $\alpha(T)$,

$$\alpha(T) = \left[1 + \kappa\left(1 - \sqrt{T/T_c}\right)\right]^2, \tag{5}$$

where T_c is the critical temperature of the fluid, and κ is related to the acentric factor ω via:

$$\kappa = 0.37464 + 1.54226\omega - 0.26992\omega^2. \tag{6}$$

The nitrogen is chosen as the working fluid in this paper. We use the acentric factor $\omega = 0.040$, which gives $\kappa \approx 0.436$. Combined with the critical properties $P_c = 3.3958$MPa and $T_c = 126.192K$, these definitions uniquely determine the temperature factor $\alpha(T)$ used in all simulations. The model parameters a and b are determined by the critical pressure P_c and critical temperature T_c of fluids[1]:

$$a = 0.45724\left(\frac{R_u^2 T_c^2}{P_c}\right), \quad b = 0.07780\left(\frac{R_u T_c}{P_c}\right). \tag{7}$$

The system of Euler equations is closed by defining the thermodynamic properties, such as the specific internal energy e and the speed of sound c. These are derived from the chosen EoS using fundamental thermodynamic relations. For detailed derivations for real fluids, refer to the work of Kim et al [52].

The final expression for internal energy e and the speed of sound squared c^2 are given by[52]

$$\begin{aligned} e(T,\rho) &= e_0(T) + \int_{\rho_0}^{\rho}\left[\frac{P}{\rho^2} - \frac{T}{\rho^2}\left(\frac{\partial P}{\partial T}\right)_\rho\right]_T d\rho, \\ c^2 &= \left(\frac{\partial P}{\partial \rho}\right)_s = \frac{c_p}{c_v}\left(\frac{\partial P}{\partial \rho}\right)_T. \end{aligned} \tag{8}$$

Here, $e_0(T)$ refers to the internal energy of the reference ideal gas state, and the subscript 0 denotes a reference ideal gas state, whose properties can be determined using standard equations, such as the NASA polynomials [18]. The terms c_p and c_v represent the specific heat capacities at constant pressure and constant volume, while the subscripts s and T denote isentropic and isothermal processes respectively. The more detailed expression of the thermodynamic derivatives, the evaluation of $c_p(T,\rho)$, $c_v(T,\rho)$, and the numerical procedures used to convert between (p, e, E) are summarized in Appendix A.

3. Numerical method

This work targets the robust simulation of real-fluid or transcritical compressible flows in which thermodynamic properties vary sharply across a small temperature range near the pseudo-boiling or Wisdom line. During the design of the algorithm for transcritical flows, there are two requirements: (i) strict conservation across shocks and contact discontinuities, and (ii) low spurious pressure-equilibrium (PE) errors when large thermodynamic gradients exist without true discontinuities. To meet both, we employ a hybrid scheme. Cells near the shock waves are updated in a conservative finite volume form using WENO-5 reconstruction [50] and a Roe-type flux solver adapted to the real-gas EoS [51]. Cells in the smooth region, transcritical region are updated in a primitive-variable form with a centered differential flux augmented by a small, upwind-biased dissipation. The primitive variables are reconstructed by WENO-5 to avoid characteristic projections through potentially ill-conditioned real-gas eigenstructures near the critical point. A conservative numerical scheme, such as the finite-volume method, is essential to ensure that the Rankine-Hugoniot jump conditions are satisfied [53]. This guarantees the correct prediction of the shock speed and strength, which is critical for physical accuracy.

Notation: Cell averages are denoted with the subscript i. Interface locations are at $x_{i\pm1/2}$. Superscripts + and - always mean right-biased and left-biased one-sided limits at an interface (e.g., $V^-_{i+1/2}$ is the value reconstructed in the left side of cell $i+1/2$). Bold capital $\mathbf{W}$ is the vector of conservative variables, $\mathbf{V}$ is vector of primitive variables, and $B(\mathbf{V}) = \partial\mathbf{F}(\mathbf{V})/\partial\mathbf{V}$ is the Jacobian of the inviscid flux written in primitive variables.

3.1. Finite volume method

The governing Euler equations in the integral conservative form for a one-dimensional control volume $[x_{i-1/2}, x_{i+1/2}]$ are given by [53]

$$\begin{aligned} &\frac{d}{dt}\int_{x_{i-1/2}}^{x_{i+1/2}} \mathbf{W}(x,t)dx \\ &\quad + \mathbf{F}\big(\mathbf{W}\big(x_{i+1/2},t\big)\big) - \mathbf{F}\big(\mathbf{W}\big(x_{i-1/2},t\big)\big) = 0, \end{aligned} \tag{9}$$

where $\mathbf{W}$ is the vector of conserved variables and $\mathbf{F}$ is the corresponding flux vector. On a uniform grid of width Δx and defining the cell-averaged value as $\mathbf{W}_i(t) = \frac{1}{\Delta x}\int_{x_{i-1/2}}^{x_{i+1/2}} \mathbf{W}(x,t)dx$, the equation becomes:

$$\frac{d\mathbf{W}_i}{dt} = -\frac{1}{\Delta x}\big(\mathbf{F}_{i+1/2} - \mathbf{F}_{i-1/2}\big), \tag{10}$$

where $\mathbf{F}_{i\pm1/2}$ represents the numerical flux at the cell interfaces.

For clarity, we first write the explicit forward-Euler update of the semi-discrete system as

$$\mathbf{W}_i^{n+1} = \mathbf{W}_i^n - \frac{\Delta t}{\Delta x}\left[\mathbf{F}_{i+\frac{1}{2}} - \mathbf{F}_{i-\frac{1}{2}}\right]. \tag{11}$$

[1] This a is the parameter computed by the critical temperature and critical pressure of corresponding fluids for the cubic EoS, rather than speed of sound.

In all computations reported in this work (including the convergence study), time advancement is performed using the third-order strong-stability-preserving Runge–Kutta method (SSP-RK3). The time step Δt is generally controlled by the Courant–Friedrichs–Lewy (CFL) condition for stability:

$$\Delta t = C_{\mathrm{cfl}} \frac{\Delta x}{S_{\max}^{(n)}}, \tag{12}$$

where $S_{\max}^{(n)} = \max_i \left\{ \left| u_i^n \right| + c_i^n \right\}$ is the maximum characteristic wave speed in the domain at time level n. The CFL number C_{cfl} depends on the specific spatial and temporal schemes used.

3.2. WENO reconstruction

In this work, we employ the WENO-5 [50] scheme to reconstruct the primitive variables directly. At each interface $x_{i+1/2}$, we compute right-biased ($v_{i+1/2}^{+}$) and left-biased ($v_{i+1/2}^{-}$) one side limits. In this subsection, superscripts + and - always mean right-biased and left-biased reconstruction at an interface.

To reconstruct a scalar component v for the left biased value $v_{i+1/2}^{-}$, a 5-point stencil $\left\{ v_{i-2}, v_{i-1}, v_i, v_{i+1}, v_{i+2} \right\}$ is used in WENO-5. This can be split into three 3-point sub-stencils:

$$\begin{aligned} S_0 &= \left\{ v_{i-2}, v_{i-1}, v_i \right\}, \\ S_1 &= \left\{ v_{i-1}, v_i, v_{i+1} \right\}, \\ S_2 &= \left\{ v_i, v_{i+1}, v_{i+2} \right\}. \end{aligned} \tag{13}$$

Each stencil is associated with a smoothness indicator $(\beta_0, \beta_1, \beta_2)$, which quantifies the variation of variables within each stencil. These indicators are computed as follows:

$$\begin{aligned} \beta_0 &= \frac{13}{12}\left(v_{i-2} - 2v_{i-1} + v_i \right)^2 + \frac{1}{4}\left(v_{i-2} - 4v_{i-1} + 3v_i \right)^2, \\ \beta_1 &= \frac{13}{12}\left(v_{i-1} - 2v_i + v_{i+1} \right)^2 + \frac{1}{4}\left(v_{i-1} - v_{i+1} \right)^2, \\ \beta_2 &= \frac{13}{12}\left(v_i - 2v_{i+1} + v_{i+2} \right)^2 + \frac{1}{4}\left(3v_i - 4v_{i+1} + v_{i+2} \right)^2. \end{aligned}$$

The raw weights α_k are determined by the smoothness indicators:

$$\alpha_0 = \frac{d_0^-}{\left(\epsilon + \beta_0 \right)^2}, \quad \alpha_1 = \frac{d_1^-}{\left(\epsilon + \beta_1 \right)^2}, \quad \alpha_2 = \frac{d_2^-}{\left(\epsilon + \beta_2 \right)^2},$$

where $\epsilon = 1 \times 10^{-6}$ is a small value added to avoid division by zero. The constants d_k^- are the ideal weights that yield fifth-order accuracy in smooth regions. For the left-biased reconstruction $v_{i+1/2}^{-}$, these are $\left\{ d_0^-, d_1^-, d_2^- \right\} = \{0.1, 0.6, 0.3\}$. The final normalized weights ω_k are then computed:

$$\omega_k = \frac{\alpha_k}{\sum_{j=0}^{2} \alpha_j}. \tag{14}$$

The reconstructed value is a weighted sum of polynomial approximations from each sub-stencil.

A similar procedure is followed for the right-biased value at interface $v_{i+1/2}^{+}$, yet using a stencil shifted to the right $\left\{ v_{i-1}, v_i, v_{i+1}, v_{i+2}, v_{i+3} \right\}$ and different ideal weights $\left\{ d_0^+, d_1^+, d_2^+ \right\} = \{0.3, 0.6, 0.1\}$.

3.3. Shock detection

In this study, shock waves are detected using the PVRS [49]. In PVRS, the Riemann problem is approximately solved by:

$$P^* = \frac{1}{2}\left(P_L + P_R \right) + \frac{1}{2}\left(u_L - u_R \right)\bar{\rho}\bar{c}, \tag{15}$$

$$u^* = \frac{1}{2}\left(u_L + u_R \right) + \frac{1}{2}\left(P_L - P_R \right)/(\bar{\rho}\bar{c}), \tag{16}$$

$$\rho_{i+\frac{1}{2}}^{L} = \rho_i + \left(u_i - u_{i+\frac{1}{2}} \right)(\bar{\rho}/\bar{c}), \tag{17}$$

$$\rho_{i+\frac{1}{2}}^{R} = \rho_{i+1} + \left(u_{i+\frac{1}{2}} - u_{i+1} \right)(\bar{\rho}/\bar{c}), \tag{18}$$

where $\bar{\rho} = \frac{1}{2}(\rho_L + \rho_R)$ and $\bar{a} = \frac{1}{2}(a_L + a_R)$ are the arithmetically averaged density and speed of sound at the interface, respectively.The propagation speeds of left and right waves are:

$$\begin{aligned} s^L_{i+\frac{1}{2}} &= \frac{\left(\rho_i u_i - \rho^L_{i+\frac{1}{2}} u_{i+\frac{1}{2}}\right)}{\rho_i - \rho^L_{i+\frac{1}{2}}}, \\ s^R_{i+\frac{1}{2}} &= \frac{\left(\rho_{i+1} u_{i+1} - \rho^R_{i+\frac{1}{2}} u_{i+\frac{1}{2}}\right)}{\rho_{i+1} - \rho^R_{i+\frac{1}{2}}}. \end{aligned} \tag{19}$$

Similar to previous research, the conservative methods are applied at cell i when:

$$\begin{aligned} &\frac{P_{i+\frac{1}{2}}}{P_i} > 1+\varepsilon \quad \text{and} \quad s^L_{i+\frac{1}{2}} < 0, \\ \text{or } &\frac{P_{i-\frac{1}{2}}}{P_i} > 1+\varepsilon \quad \text{and} \quad s^R_{i-\frac{1}{2}} < 0, \end{aligned} \tag{20}$$

where the parameter ε can be selected within the range $(0, 0.1)$. In this paper, $\varepsilon = 0.05$ is used.

3.4. Conservative update

For the cells near shock waves, a standard finite-volume WENO-5 scheme with Roe-type real-gas flux is used to update the conservative variable. Primitive variables $\mathbf{V}$ are reconstructed to obtain left ($\mathbf{V}_L = \mathbf{V}^+$) and right ($\mathbf{V}_R = \mathbf{V}^-$) states at interfaces, which are then converted to conservative variables $\mathbf{W}_L$ and $\mathbf{W}_R$. The Roe approximate Riemann solver designed for the real gas is used for the Roe flux. For more details, readers can refer to previous work [51]. It is proved in previous research[37–39] that, compared with primitive form, the conservative form can maintain an accurate prediction of the speed and strength of shock waves.

3.5. Primitive update

For cells in the smooth region, we discretize the non-conservative, quasi-linear form of the Euler equations:

$$\frac{\partial \mathbf{V}}{\partial t} + \mathbf{B}(\mathbf{V})\frac{\partial \mathbf{V}}{\partial x} = 0, \tag{21}$$

where $\mathbf{V} = [\rho, u, P]^T$ is the vector of primitive variables, and $\mathbf{B}(\mathbf{V})$ is the Jacobian matrix of primitive equations. The spatial term $\mathcal{L}_v = -\mathbf{B}(\mathbf{V})\partial_x \mathbf{V}$ is handled by our proposed CDHD approach. This method split the flux into a central differential term and an upwind dissipative term:

$$\mathcal{L}_v = \underbrace{\mathcal{L}_v^{\text{central}}}_{\text{accuracy}} + \underbrace{\mathcal{L}_v^{\text{diss}}}_{\text{stability}}. \tag{22}$$

The central term is approximated using the WENO-5 reconstructed interface state:

$$\begin{aligned} \partial_x \mathbf{V}\big|_i &\approx \frac{\mathbf{V}^-_{i+1/2} - \mathbf{V}^+_{i-1/2}}{\Delta x}, \\ \mathcal{L}_v^{\text{central}}(i) &= -B(\mathbf{V}_i)\frac{\mathbf{V}^-_{i+1/2} - \mathbf{V}^+_{i-1/2}}{\Delta x}. \end{aligned} \tag{23}$$

Here $\mathbf{V}^-_{i+1/2}$ denotes the left-biased reconstruction at $x_{i+1/2}$ and $\mathbf{V}^+_{i-1/2}$ the right-biased reconstruction at $x_{i-1/2}$. With this choice, both interface values are obtained from the same symmetric five-point stencil $\{i-2, i-1, i, i+1, i+2\}$ around cell i, so Eq. (23) is a two-point centered difference on staggered location with a compact stencil rather than an upwind operator. In smooth regions WENO-5 yields $\mathbf{V}^{\pm}_{i\pm1/2} = \mathbf{V}(x_{i\pm1/2}) + \mathcal{O}(\Delta x^5)$, as analysed in Section 4.2.

Given that this is a two-point centered difference on staggered locations, its truncation error is $O(\Delta x^2)$ even though the individual interface states are fifth-order accurate. If desired, a higher order central derivative can be utilized without changing the rest of the formulation.

To stabilize this centered operator with a physically consistent upwind bias, we add Osher-type (DOTRS) [54,55] interface fluctuations built from a path-conservative treatment of the non-conservative product $\mathbf{B}(\mathbf{V})\partial_x \mathbf{V}$.

At an interface $x_{i+1/2}$, we denote the WENO reconstructed left and right states by:

$$\mathbf{V}_L = \mathbf{V}^-_{i+1/2}, \quad \mathbf{V}_R = \mathbf{V}^+_{i+1/2}, \tag{24}$$

and connect them by the straight path $\mathbf{\Psi}(s) = \mathbf{V}_L + s\,(\mathbf{V}_R - \mathbf{V}_L),\ s \in [0,1]$. The characteristic splitting $\mathbf{B}^{\pm} = \frac{1}{2}(\mathbf{B} \pm |\mathbf{B}|)$ (with $|\mathbf{B}| = \mathbf{R}|\Lambda|\mathbf{R}^{-1}$) then yields the DOTRS fluctuations as:

$$\begin{aligned}\mathbf{H}^{\pm}_{i+1/2} &= \int_0^1 \mathbf{B}^{\pm}(\mathbf{\Psi}(s))\,\frac{\partial \mathbf{\Psi}}{\partial s}(s)\,\mathrm{d}s \\ &= \left(\int_0^1 \mathbf{B}^{\pm}(\mathbf{\Psi}(s))\,\mathrm{d}s\right)(\mathbf{V}_R - \mathbf{V}_L),\end{aligned} \tag{25}$$

which we evaluate with a 3 -point Gauss-Legendre rule. Summing the contributions from the two adjacent interfaces gives the dissipation in divergence form:

$$\mathcal{L}_v^{\mathrm{diss}}(i) = -\frac{1}{\Delta x}\left(\mathbf{H}^{-}_{i+1/2} + \mathbf{H}^{+}_{i-1/2}\right). \tag{26}$$

We note that, in the primitive update, total energy is not evolved from a conservative flux, so exact discrete conservation is not enforced. However, the particular CDHD construction strongly limits the resulting conservation error. The central contribution $\mathcal{L}_v^{\mathrm{central}}$ in Eq. (23) corresponds to a centered discretization of the quasi-linear Euler system and advects the primitive variables with very low numerical diffusion. When the density and momentum are transported in this way, the implied total energy obtained from (ρ, u, p) and the EoS satisfy the conservative energy balance up to the truncation error of the central derivative. The DOTRS-based dissipation $\mathcal{L}_v^{\mathrm{diss}}$ in Eq. (26) only adds an $\mathcal{O}(\Delta x^4)$ correction in smooth regions, so its contribution to the global energy budget is much smaller than that of a first-order upwind formulation in which the full flux is replaced by a dissipative Riemann solver.

In smooth regions, the jump $\mathbf{V}_R - \mathbf{V}_L = O(\Delta x^5)$ for WENO-5, so that $\mathcal{L}_v^{\mathrm{diss}} = O(\Delta x^4)$.[2] Thus the dissipation is subdominant compared to the central term. In fact, the dissipation acts as a gentle upwind stabilization proportional to the spectral radius $|u| + a$, without degrading the formal order of the chosen central derivative.

In transcritical regions, however, the central term alone is not sufficient to stabilize the primitive update: the strong nonlinearity of the real-gas EoS makes the system highly sensitive to small inconsistencies between the discretized equations and the thermodynamic closure. The DOTRS-based dissipative term provides the missing upwind bias in characteristic space, so that any residual mismatch between the transported primitive variables and the EoS is damped rather than amplified. Together with the PVRS-based shock sensor in Section 3.3, which switches to the fully conservative WENO–Roe scheme in cells containing genuine discontinuities, this characteristic-based dissipation is the key mechanism that suppresses the spurious pressure oscillations usually observed near the pseudo-boiling line when thermal properties change dramatically.

In the present work we distinguish between two closely related formulations. The first is a primitive-only CDHD scheme, which applies the Osher-type dissipation directly to the primitive variables on the entire domain. This formulation is low-dissipative and relatively inexpensive, and is intended as the default solver for transcritical flows without strong shocks. The second is the hybrid CDHD + Roe scheme described above, in which a PVRS-based sensor activates a conservative WENO–Roe update only in cells affected by strong compressive waves, while the primitive-only CDHD update is used elsewhere. In this setting the hybrid scheme is only meant to account for shock waves and other localized non-smooth features, whereas smooth regions are handled by the cheaper primitive-only formulation.

4. Error analysis

In this section, we provide a detailed mathematical justification for the behavior of the primitive update in smooth regions. We analyze the truncation error in the central term $\mathcal{L}_v^{\mathrm{central}}$, which reveals a second-order accuracy, and the scaling of the state jump $d\mathbf{V} = \mathbf{V}_R - \mathbf{V}_L$, which leads to DOTRS fluctuations $\mathbf{H}^{\pm} = O(\Delta x^5)$ and a dissipative term $\mathcal{L}_v^{\mathrm{diss}} = O(\Delta x^4)$. The dissipation magnitude is small enough not to influence the overall order of accuracy, namely the error from the central term dominates. We start by revisiting the key elements of WENO reconstruction and DOTRS, and then proceed with Taylor expansions and error analysis to reveal the behavior. By providing a detail error analysis, one can derive a higher order central flux easily.

4.1. WENO-5 Reconstruction and state jump scaling

The WENO-5 scheme, introduced by Jiang and Shu [50], reconstructs interface values from cell-averaged primitives $\mathbf{V}_i$ to achieve fifth-order accuracy in smooth regions. For a smooth scalar field $v(x)$, the cell average in cell i (centered at x_i, with width Δx) is:

$$\bar{v}_i = \frac{1}{\Delta x}\int_{x_{i-1/2}}^{x_{i+1/2}} v(\xi)\,d\xi = v(x_i) + O(\Delta x^2), \tag{27}$$

where the Taylor expansion around x_i shows that the approximation error is $O(\Delta x^2)$.

WENO5 computes left- ($v^-_{i+1/2}$) and right-biased ($v^+_{i+1/2}$) approximations at interface $x_{i+1/2}$ using a nonlinear weighted average of three candidate polynomials over stencils such that, in smooth regions, the combined reconstruction satisfies

$$v^{\pm}_{i+1/2} = v(x_{i+1/2}) + O(\Delta x^5). \tag{28}$$

At interface $i + 1/2$ we set:

[2] For more details of the derivative process about the order of accuracy, please refer to the next section.

- $V_L = V_i^+$: Right-biased reconstruction from the left cell i, approximating $V(x_{i+1/2}) + O(\Delta x^5)$.
- $V_R = V_{i+1}^-$: Left-biased from the right cell $i+1$, also approximating $V(x_{i+1/2}) + O(\Delta x^5)$.

In smooth regions, writing

$$V_L = V\left(x_{i+1/2}\right) + c_L \Delta x^5 + O\left(\Delta x^6\right), \tag{29a}$$

$$V_R = V\left(x_{i+1/2}\right) + c_R \Delta x^5 + O\left(\Delta x^6\right), \tag{29b}$$

with (generally different) constants c_L and c_R, the subtraction of Eq. (29a) and Eq. (29b) yields $dV = (c_R - c_L)\Delta x^5 + O\left(\Delta x^6\right) = O\left(\Delta x^5\right)$. Lower-order terms are canceled because the scheme is provably fifth-order accurate at the interface. Thus, the jump is

$$dV := V_R - V_L = O\left(\Delta x^5\right). \tag{30}$$

Near discontinuities the WENO nonlinearity lowers the order and dV can be $O(1)$. Our hybrid method switches computations in such cells to conservative update, and thus the primitive update is used only where the $O\left(\Delta x^5\right)$ scaling holds.

4.2. Central flux truncation error

We analyze the truncation error of the central part of the primitive update

$$\mathcal{L}_v^{\text{central}}(i) = -B\left(\mathbf{V}_i\right) \frac{\mathbf{V}_{i+1/2}^- - \mathbf{V}_{i-1/2}^+}{\Delta x} \tag{31}$$

in smooth regions. Two independent $O(\Delta x^2)$ mechanisms govern the accuracy: (1) the derivative approximation from two midpoint values, and (2) the use of $B\left(\mathbf{V}_i\right)$ (a cell averaged value) in place of $B\left(\mathbf{V}(x_i)\right)$ (an accurate point value).

4.2.1. Central difference from midpoints is second order

Let V be a smooth scalar component. By using exact interface values, one can arrive:

$$\begin{aligned} &\frac{V\left(x_{i+1/2}\right) - V\left(x_{i-1/2}\right)}{\Delta x} \\ &= V'\left(x_i\right) + \frac{\Delta x^2}{24} V^{(3)}\left(x_i\right) + O\left(\Delta x^4\right). \end{aligned} \tag{32}$$

Thus, the central-difference operator built from the two adjacent midpoints is inherently second order, regardless of how accurately those midpoint values are obtained.

When employing WENO-5 reconstruction in the smooth region, one observes

$$V_{i\pm1/2}^{\pm} = V\left(x_{i\pm1/2}\right) + O\left(\Delta x^5\right), \tag{33}$$

so the reconstruction error contributes only

$$\frac{\left[O\left(\Delta x^5\right)\right] - \left[O\left(\Delta x^5\right)\right]}{\Delta x} = O\left(\Delta x^4\right), \tag{34}$$

which is subdominant to the $O(\Delta x^2)$ from the central difference itself.

4.2.2. Coefficient mismatch of $B\left(\mathbf{V}_i\right)$ and $B\left(\mathbf{V}(x_i)\right)$ is also $O(\Delta x^2)$

$\mathbf{V}_i$ is a cell average $\mathbf{V}_i = \mathbf{V}\left(x_i\right) + O\left(\Delta x^2\right)$ by smoothing B:

$$B\left(\mathbf{V}_i\right) = B\left(\mathbf{V}\left(x_i\right)\right) + O\left(\Delta x^2\right). \tag{35}$$

By adding and subtracting the exact midpoint values in Eq. (31), one can obtain

$$\begin{aligned} \mathcal{L}_v^{\text{central}}(i) = &- \underbrace{B\left(\mathbf{V}\left(x_i\right)\right)}_{\text{exact coeff.}} \underbrace{\frac{V\left(x_{i+1/2}\right) - V\left(x_{i-1/2}\right)}{\Delta x}}_{\text{2-pt central diff}} \\ &- \left(B\left(\mathbf{V}_i\right) - B\left(\mathbf{V}\left(x_i\right)\right)\right) \frac{\mathbf{V}_{i+1/2}^- - \mathbf{V}_{i-1/2}^+}{\Delta x} \\ &- B\left(\mathbf{V}\left(x_i\right)\right) \left(\frac{\mathbf{V}_{i+1/2}^- - \mathbf{V}_{i-1/2}^+ - \frac{V\left(x_{i+1/2}\right) - V\left(x_{i-1/2}\right)}{\Delta x}}{\Delta x} \right). \end{aligned} \tag{36}$$

In the first line of the above Eq. (36), the second-order central difference produces an $O(\Delta x^2)$ error. In the second line, $B\left(\mathbf{V}_i\right) - B\left(\mathbf{V}\left(x_i\right)\right) = O\left(\Delta x^2\right)$ times an $O(1)$ gradient also generates an $O(\Delta x^2)$ error. In the third line, reconstruction defects contribute only $O\left(\Delta x^4\right)$ error.Therefore,

$$\mathcal{L}_v^{\text{central}}(i) = -B\left(\mathbf{V}\left(x_i\right)\right) \partial_x \mathbf{V}\left(x_i\right) + O\left(\Delta x^2\right), \tag{37}$$

so the overall truncation error of the central term is $O(\Delta x^2)$. Importantly, this second-order behavior is not due to WENO reconstruction (which is 5th order at the interfaces), but to (a) the two-midpoint central differencing and (b) the use of $B(\mathbf{V}_i)$ evaluated at a cell average.

4.3. Dissipative term scaling

Let $d\mathbf{V} = \mathbf{V}_R - \mathbf{V}_L$ and the straight-line path $\Psi(s) = \mathbf{V}_L + sd\mathbf{V}, s \in [0,1]$. The DOTRS[54,55] fluctuations are:

$$\mathbf{H}^{\pm} = \int_0^1 B^{\pm}(\Psi(s))ds d\mathbf{V}, \tag{38}$$

$$B^{\pm}(\mathbf{V}) = \frac{1}{2}(B(\mathbf{V}) \pm |B(\mathbf{V})|), \tag{39}$$

$$|B| = R|\Lambda|R^{-1}, \tag{40}$$

with eigenvalues $\Lambda = \mathrm{diag}(u-c, u, u+c)$ and $\Psi(s) = \mathbf{V}_L + sd\mathbf{V}, s \in [0,1]$.

Throughout this section we assume B is C^2 (twice continuously differentiable) and that the eigen structure of $B(\mathbf{V})$ is smooth along the path $\Psi(s)$ (no eigenvalue sign change), so that $|B|$ and $B^{\pm} = 1/2(B \pm |B|)$ are differentiable.

Define D as the Fréchet derivative (directional derivative of a matrix-valued function):

$$DB^{\pm}(\mathbf{V})[\delta\mathbf{V}] = \lim_{\tau\to 0} \frac{B^{\pm}(\mathbf{V}+\tau\delta\mathbf{V}) - B^{\pm}(\mathbf{V})}{\tau}. \tag{41}$$

The small-jump expansion can be derived as follows. Define $f(s) = B^{\pm}(\Psi(s))$. By Taylor expansion in s and the chain rule, one can arrive:

$$\begin{aligned} f(s) =& B^{\pm}(\mathbf{V}_L) + sDB^{\pm}(\mathbf{V}_L)[d\mathbf{V}] \\ &+ \frac{1}{2}s^2 D^2 B^{\pm}(\mathbf{V}_L)[d\mathbf{V}, d\mathbf{V}] + O(\|d\mathbf{V}\|^3). \end{aligned} \tag{42}$$

By integrating the above equation, we obtain

$$\begin{aligned} \int_0^1 f(s)ds =& B^{\pm}(\mathbf{V}_L) + \frac{1}{2}DB^{\pm}(\mathbf{V}_L)[d\mathbf{V}] \\ &+ \frac{1}{6}D^2 B^{\pm}(\mathbf{V}_L)[d\mathbf{V}, d\mathbf{V}] + O(\|d\mathbf{V}\|^3). \end{aligned} \tag{43}$$

Multiplying Eq. (43) by $d\mathbf{V}$ gives

$$\mathbf{H}^{\pm} = B^{\pm}(\mathbf{V}_L)d\mathbf{V} + \frac{1}{2}DB^{\pm}(\mathbf{V}_L)[d\mathbf{V}]d\mathbf{V} + O(\|d\mathbf{V}\|^3). \tag{44}$$

Hence, $\|\mathbf{H}^{\pm}\| \le C_1\|d\mathbf{V}\| + C_2\|d\mathbf{V}\|^2$, i.e. linear in $d\mathbf{V}$ to the leading order.

By using WENO-5 reconstruction, the reconstructed interface states in smooth region satisfy:

$$\begin{aligned} \mathbf{V}_L &= \mathbf{V}(x_{i+1/2}) + O(\Delta x^5), \\ \mathbf{V}_R &= \mathbf{V}(x_{i+1/2}) + O(\Delta x^5). \end{aligned} \tag{45}$$

Thus, $d\mathbf{V} = O(\Delta x^5)$. With the operator norm being controlled by $\|\mathbf{B}(\mathbf{V}_{\mathrm{avg}})\| \lesssim C(|u|+c)$, one can arrive

$$\begin{aligned} &\mathbf{H}^{\pm} = O(\Delta x^5) \quad \text{and} \\ &\mathcal{L}_v^{\mathrm{diss}}(i) = -\frac{1}{\Delta x}\left(\mathbf{H}^-_{i+1/2} + \mathbf{H}^+_{i-1/2}\right) = O(\Delta x^4). \end{aligned} \tag{46}$$

Thus the dissipation is high-order small and does not limit accuracy when combined with the central term. The total $\mathcal{L}_v = \mathcal{L}_v^{\mathrm{central}} + \mathcal{L}_v^{\mathrm{diss}}$ thus has an overall truncation error $O(\Delta x^2)$ in smooth regions, remaining spatial accuracy to the second order.

4.4. The role of DOTRS in first-order vs. high-order schemes

The function of the DOTRS dissipation changes dramatically with the order of the underlying scheme.

4.4.1. Role in first-Order schemes

In a first-order Godunov-type scheme, states are assumed to be piecewise constant, so $\mathbf{V}_L = \mathbf{V}_i$ and $\mathbf{V}_R = \mathbf{V}_{i+1}$. Jumps across interfaces are large ($d\mathbf{V} = O(1)$). Here, the DOTRS integral acts as the primary Riemann solver, providing the full upwind flux necessary for stability and physical resolution. The resulting spatial discretization $L_v(i) = -\frac{1}{\Delta x}(H^-_{i+1/2} + H^+_{i-1/2})$ is first-order accurate.

4.4.2. Role in this high-Order scheme

In our high-order method, the primary advection is handled by the accurate central flux term. The role of DOTRS is reduced to that of a targeted stabilizer. Given that high-order reconstruction ensures the interface jump $d\mathbf{V}$ is very small ($O(\Delta x^5)$) in smooth regions, the DOTRS fluctuation $\mathbf{H}^{\pm}$ also becomes minor. For a small $d\mathbf{V}$, the dissipation behaves similarly to a local Lax-Friedrichs scheme, whereas with a crucial difference that its magnitude is scaled by the high-order jump. The resulting dissipative term in the final update $\mathcal{L}_v^{\text{diss}}$ is $O(\Delta x^4)$. This dissipation is numerically small enough such that it vanishes faster than the error of the second-order central term as the grid is refined. Therefore, it successfully provides stabilization against oscillations without affecting the formal second-order accuracy of the overall scheme.

In the present work we therefore obtain a second-order accurate central term $\mathcal{L}_v^{\text{central}}$. More generally, the DOTRS path-integral dissipation introduced in Section 4.3 depends on the size of the reconstructed jump $d\mathbf{V} = \mathbf{V}_R - \mathbf{V}_L$. With WENO-5 we have $d\mathbf{V} = O(\Delta x^5)$ in smooth region, which yields a dissipative contribution $\mathcal{L}_v^{\text{diss}} = O(\Delta x^4)$ and thus does not limit the overall accuracy. If one wish to employ a high-order centered derivative of order p, it suffices to choose an interface reconstruction of order $r \geq p+1$, so that $\mathcal{L}_v^{\text{diss}} = O(\Delta x^{r-1})$ remains of order at least p. Our current choice of WENO-5 ($r = 5$) would therefore also be compatible with a fourth-order operator in Eq. (23).

The above argument extends directly to other reconstruction orders. If the interface reconstruction is of order r rather than five, then in smooth regions $\mathbf{V}_L, \mathbf{V}_R = \mathbf{V}(x_{i+1/2}) + O(\Delta x^r)$ and hence $d\mathbf{V} = O(\Delta x^r)$. The expansion in Eqs. (38)–(44) then implies $\mathbf{H}^{\pm} = O(\Delta x^r)$ and $\mathcal{L}_v^{\text{diss}} = O(\Delta x^{r-1})$. If the central derivative is of order p, choosing $r \geq p+1$ ensures that the DOTRS dissipation remains subdominant and does not reduce the formal spatial order.

Because the conservative and primitive formulations are mathematically equivalent at the continuous level, any conservation error arises purely from the spatial discretization. The analysis above shows that in smooth regions the non-conservative part of the CDHD operator is of order $\mathcal{O}(\Delta x^2)$ from the central term with only an $\mathcal{O}(\Delta x^4)$ contribution from the DOTRS dissipation. Therefore, the discrepancy between the discrete primitive update and the conservative energy equation is of the same order as the truncation error of a standard second-order finite-volume scheme.

5. Result and discussion

In this section, a series of 1D and 2D numerical tests are undertaken to illustrate the accuracy and stability of the proposed scheme. The transcritical nitrogen is adopted as the working fluid in all of the test cases with the thermodynamic properties of fluids obtained by PR EoS. The numerical results are compared with available standard solutions. For a low magnitude dissipation, the WENO-5 reconstruction is used in all cases. The following cases show that the numerical scheme proposed in this paper can achieve an accurate, oscillation free simulation in transcritical regions.

5.1. 1-D transcritical advection cases

5.1.1. Result of CDHD scheme

A one-dimensional transcritical advection case is considered in a periodic domain $\Omega \in [0, 1]$ m. The initial conditions consist of a sharp but continuous temperature gradient centered within the domain, while the velocity and pressure fields are spatially uniform. The setup mimics a droplet in a transcritical environment, which is defined as

$$\begin{aligned} T(x) &= T_l \\ &\quad + \frac{T_r - T_l}{2}\left[\tanh\left(\frac{x-0.25}{\eta}\right) + \tanh\left(\frac{-(x-0.75)}{\eta}\right)\right], \\ u(x) &= 100 \quad (\text{m/s}), \qquad p(x) = 4.0\times 10^6 \quad (\text{Pa}), \end{aligned} \tag{47}$$

where, $T_L = 200$ K and $T_R = 100$ K are the left and right reference temperatures, respectively; $\eta = 0.1$ is a smoothing parameter controlling the width of the temperature transition. The density field $\rho(x)$ is computed using the PR EoS.

Because the velocity and pressure are spatially uniform and periodic boundary conditions are imposed, the exact solution is obtained by advecting the initial profiles at constant speed. At the reporting time $t = 0.1$ s (ten traversals of the periodic domain), this analytical solution coincides with the initial condition, which is therefore used as the reference solution in Fig. 2.

The proposed CDHD method with a WENO-5 reconstruction is validated against a transcritical convection problem with a known analytical solution. The numerical results at the simulation time $t = 0.1$ s, corresponding to 10 periods of convection, are presented in Fig. 2. All results are simulated with 512 grid points.

For the velocity and pressure fields, both the CDHD WENO-5 and the first-order DOTRS schemes demonstrate an excellent agreement with the analytical solution. Both methods achieve a robust simulation, accurately maintaining the constant velocity of 100 m/s and pressure of 4.0 MPa across the entire spatial domain. However, significant differences emerge in the temperature and density profiles. The density field exhibits more rapid variations due to the nonlinear thermodynamic effect near the critical point. The CDHD WENO-5 method accurately reproduces both the density and temperature profiles, preserving the sharpness of transitions without introducing spurious oscillations. In contrast, the first-order DOTRS scheme results in noticeable smearing of the interface, limiting its usage in resolving sharp gradients.

Overall, the CDHD method with WENO-5 reconstruction demonstrates superior accuracy and robustness in simulating transcritical flows, particularly in capturing the nonlinearities arising from thermodynamic properties. The method delivers robust performance

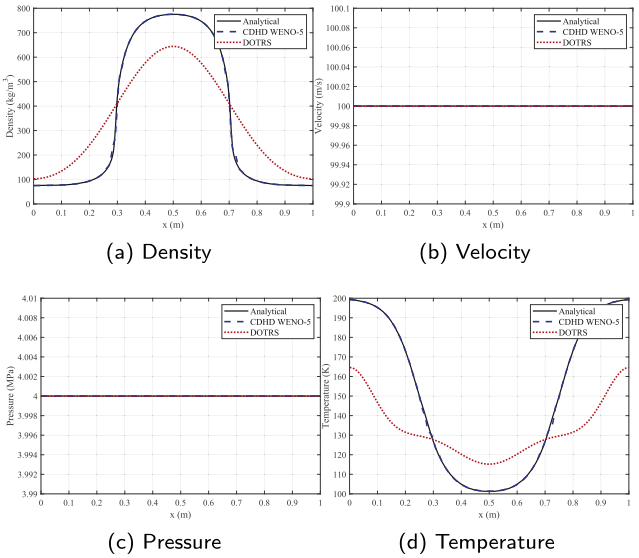

Fig. 2. Comparison of numerical results from the CDHD WENO-5 and the first-order DOTRS schemes with the analytical solution for the 1-D transcritical advection case at $t = 0.1$ s (ten domain traversals) using 512 grid points. Profiles of (a) density, (b) velocity, (c) pressure, and (d) temperature are shown. The CDHD WENO-5 scheme shows an excellent agreement with the analytical solution, while the DOTRS scheme exhibits significant numerical smearing in the density and temperature profile.

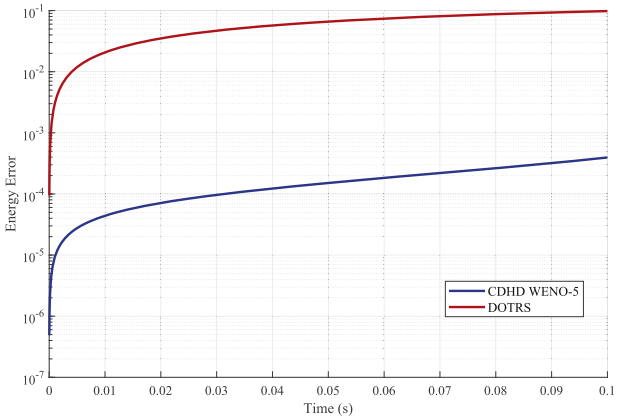

Fig. 3. Temporal evolution of the relative energy conservation error for the CDHD WENO-5 and the first-order DOTRS schemes, plotted on a semi-logarithmic scale. The error for the proposed CDHD WENO-5 scheme remains below 0.04% at the final time of $t = 0.1$ s, while the error for the DOTRS scheme grows to approximately 10% at the same instant.

across all evaluated fields including density, velocity, pressure, and temperature. Our work provides a new strategy for the further development of the high-order scheme for transcritical flows.

5.1.2. Energy conservation error

The primitive method has long been criticized for violating the law of energy conservation. However, the results from the proposed CDHD WENO-5 scheme demonstrate substantial improvements in energy conservation. We further examine the temporal evolution of the relative energy conservation error, defined as $\epsilon_E = \left|\frac{E(t)-E(0)}{E(0)}\right|$, where $E(t)$ is the integrated total energy at time t. Fig. 3 presents this error metric over the simulation duration from $t = 0$ to $t = 0.1$s (equivalent to 10 convection periods) on a semi-logarithmic scale.

The results clearly demonstrate the superior performance of the proposed method in conserving energy. The CDHD WENO-5 scheme maintains a low energy error throughout the simulation, reaching a final error value of approximately 3.95×10^{-4} at $t = 0.1$ s. This corresponds to an error of less than 0.04 %, indicating a high degree of energy conservation suitable for long-duration simulations. In contrast, the first-order DOTRS scheme exhibits a significantly larger error that grows to about 10 % by the final time point. This direct comparison reveals that the energy conservation error of the CDHD WENO-5 scheme is over two orders of magnitude lower than that of the DOTRS scheme at the end of the simulation.

Table 1
Grid-convergence results for the true relative L_1 errors $\epsilon^{\text{rel}}_{L_1}$ defined in Eq. (48). Errors are evaluated at $t = L/|u| = 0.01$ s (one domain traversal). For this convergence study, we use a fixed time step Δt chosen from the finest grid based on the initial CFL condition (CFL= 0.8) and apply the same Δt for all coarser grids.

N_x	dx	$\epsilon^{\text{rel}}_{L_1}(\rho)$	Order	$\epsilon^{\text{rel}}_{L_1}(\rho u)$	Order	$\epsilon^{\text{rel}}_{L_1}(E)$	Order
32	3.1250×10^{-2}	5.0565×10^{-2}	N/A	5.0565×10^{-2}	N/A	5.8736×10^{-2}	N/A
64	1.5625×10^{-2}	2.3979×10^{-2}	1.0764	2.3979×10^{-2}	1.0764	2.6611×10^{-2}	1.1422
128	7.8125×10^{-3}	7.7455×10^{-3}	1.6304	7.7455×10^{-3}	1.6304	8.4986×10^{-3}	1.6467
256	3.9062×10^{-3}	2.7443×10^{-3}	1.4969	2.7443×10^{-3}	1.4969	2.9446×10^{-3}	1.5291
512	1.9531×10^{-3}	7.5258×10^{-4}	1.8665	7.5258×10^{-4}	1.8665	7.8900×10^{-4}	1.9000
1024	9.7656×10^{-4}	1.6704×10^{-4}	2.1717	1.6704×10^{-4}	2.1717	1.7106×10^{-4}	2.2055

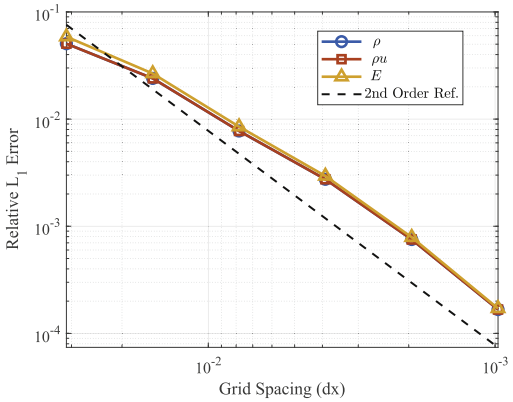

Fig. 4. Grid convergence of the true relative L_1 errors $\epsilon^{\text{rel}}_{L_1}$ for ρ, ρu, and E (Eq. (48)), evaluated at $t = 0.01$ s (one domain traversal). For the convergence study, a fixed time step Δt (computed from the finest grid using CFL= 0.8 at $t = 0$) is used for all grids so that the reported rates reflect spatial accuracy. The dashed line indicates a second-order reference slope.

The marked difference between the CDHD and DOTRS results can be understood from the structure of the numerical fluxes. In the first-order DOTRS scheme the entire advection operator is replaced by a path-integral Riemann solver, so the numerical dissipation is $\mathcal{O}(\Delta x)$ and directly perturbs the total-energy balance. In CDHD, only a small high-order correction is computed from DOTRS, while the main transport of (ρ, u, p) is performed by the low-dissipation central term. In smooth regions the dissipative term is proportional to an $\mathcal{O}(\Delta x^5)$ jump in the reconstructed state, so it contributes an $\mathcal{O}(\Delta x^4)$ perturbation to the total energy. Consequently, the primitive-variable update in the proposed scheme introduce a smaller energy error than that of the fully upwind DOTRS discretization at the same solution.

5.1.3. Convergence test

For each conserved variable $q \in \{\rho, \rho u, E\}$ we report the relative L_1 error,

$$\epsilon^{\text{rel}}_{L_1}(q) = \frac{\sum_j \left| q_j^{\text{num}} - q_j^{\text{exact}} \right|}{\sum_j \left| q_j^{\text{exact}} \right|}, \tag{48}$$

where q_j^{num} and q_j^{exact} denote the numerical and analytical solutions at grid point x_j. All errors reported in Table 1 and Fig. 4 use this relative metric.

This test is time-dependent, so both spatial and temporal discretization errors may be present. In order to assess *spatial* accuracy without contamination from changing temporal errors across grids, we adopt a fixed-Δt strategy: we compute Δt from the CFL condition (CFL= 0.8) on the *finest* grid using the initial maximum wave speed, and then use this same Δt for all coarser grids. Time integration is performed using the third-order strong-stability-preserving Runge–Kutta method (SSP-RK3). The final time corresponds to one domain traversal, $t = L/|u| = 0.01$ s.

As shown in Table 1 and Fig. 4, the scheme exhibits near second-order convergence on sufficiently fine meshes. The slightly reduced rates on the coarsest grids are attributed to pre-asymptotic behavior due to under-resolution of the steep transition region in the initial profile. For practical reference, the relative L_1 error is below 0.3% at $N_x = 256$ and decreases to $\mathcal{O}(10^{-4})$ at $N_x = 1024$.

5.1.4. Role of high-order dissipation

To isolate the effect of the dissipative term, we repeat the transcritical advection test case using only the central differential flux for $\partial_x \mathbf{V}$, omitting the high-order dissipative stabilization. The results in Figs. 5 after 600 time steps with CFL = 0.8 clearly demonstrate

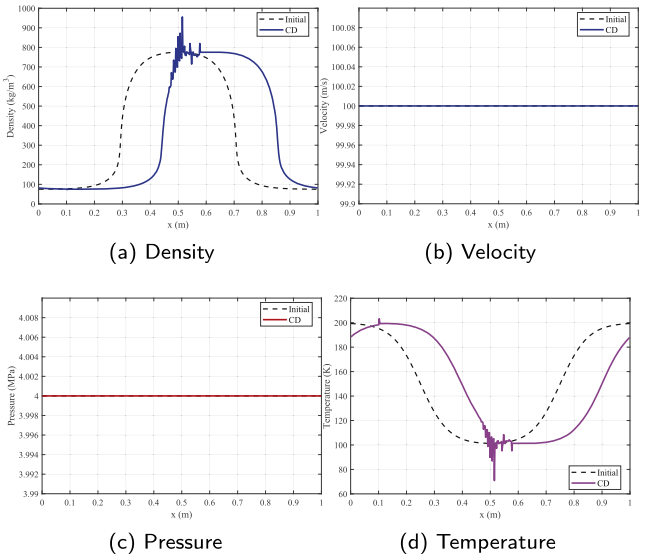

Fig. 5. Profiles of density, velocity, pressure and temperature for 1-D transcritical advection case when only using the central differential interface flux. Oscillation will be accumulated in time and blow up the simulation quickly.

the necessity of dissipation in the transcritical regime. The small magnitude dissipation proposed in this paper can greatly stabilize the simulation process.

As shown in Fig. 5, the central difference scheme without stabilization develops severe numerical instabilities. The density field exhibits spurious oscillations and overshoots near the steep gradient region, with spurious wiggles corrupting the solution throughout the domain. Similarly, the temperature field displays significant nonphysical oscillations that grow rapidly in time. In contrast, the velocity and pressure fields remain relatively stable, staying close to their initial uniform states with only minor perturbations.This selective instability pattern is characteristic of transcritical flow physics, where small perturbations in thermodynamic properties can trigger rapid growth of numerical modes.

These results demonstrate that a small amount of high-order, characteristic-based dissipation is essential for stabilizing the primitive variable update in transcritical flows. The dissipative term proposed in this work provides this stabilization without compromising the leading-order accuracy of the scheme, as evidenced by the convergence analysis presented earlier.

5.2. 1-D shock tube problems

This section demonstrates the capability of the hybrid scheme in this work for accurately capturing the strength and propagation speed of shock waves through a 1-D shock tube test case. We consider a computational domain of $x \in [0, 1]$ m with transmissive boundary conditions applied at both ends. All simulations employ a CFL number 0.8 and are run until $t = 5 \times 10^{-4}$ s. The initial conditions for the transcritical shock tube problem are specified as a Riemann problem with left and right states:

$$\begin{bmatrix} \rho_l \\ u_l \\ p_l \end{bmatrix} = \begin{bmatrix} 800\ \text{kg/m}^3 \\ 0\ \text{m/s} \\ 60e6\ \text{Pa} \end{bmatrix}, \qquad \begin{bmatrix} \rho_r \\ u_r \\ p_r \end{bmatrix} = \begin{bmatrix} 80\ \text{kg/m}^3 \\ 0\ \text{m/s} \\ 6e6\ \text{Pa} \end{bmatrix}. \tag{49}$$

This configuration creates a strong pressure and density ratio of the left and right sides in the simulation domain, establishing conditions that span the transcritical regime and challenge numerical methods with steep gradients and rapid thermodynamic variations.

Fig. 6 presents the computed density, velocity, pressure, and temperature profiles without using any limiter or filter. The solutions demonstrate the adaptive scheme has the ability to resolve the complex wave structure typical of transcritical shock tubes, including shock waves, contact discontinuities, and expansion regions, while maintaining sharp interfaces without spurious oscillations.

In this test, the PVRS-based sensor defined in Section 3.3 is used at every time step to classify each cell as either “shock” (conservative update) or “smooth” (primitive update). Cells satisfying condition Eq. (20) are advanced using the conservative WENO-Roe scheme of Section 3.4, whereas all remaining cells are updated with the primitive CDHD scheme of Section 3.5. Fig. 7 displays the resulting switching indicator at the final time: the conservative branch is activated only in a narrow region surrounding the shock, while the rarefaction, contact discontinuity, and far-field regions are updated using the primitive formulation.

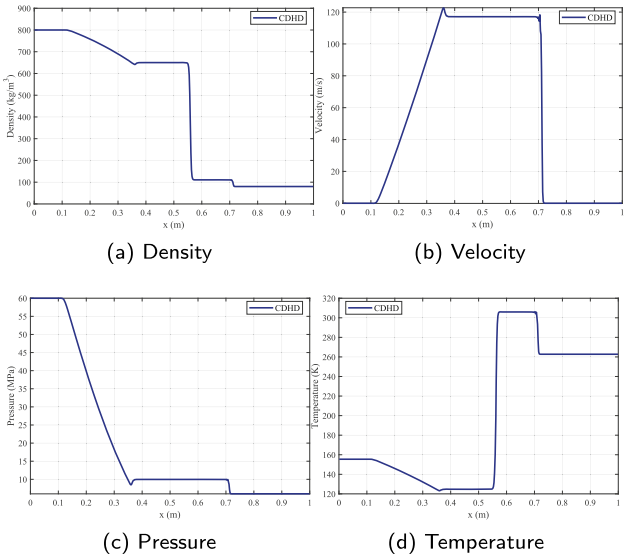

Fig. 6. Profiles of density, velocity, pressure and temperature for 1-D shock tube problems.

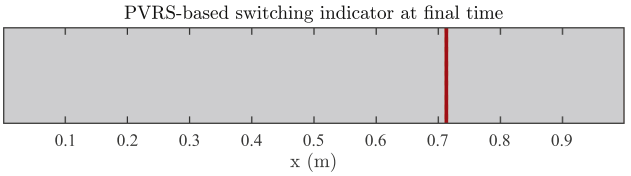

Fig. 7. PVRS-based switching indicator at the final time for the 1D shock-tube test. Red cells are updated with the conservative WENO-Roe scheme, gray cells with the primitive CDHD scheme.

5.3. 1-D shock-temperature-ramp interaction

The previous shock tube example isolate either a single, nearly discontinuous shock or a smooth transcritical advection problem. To demonstrate how hybrid scheme behaves when these features coexist and evolve in time, we now consider a one-dimensional configuration where a shock wave interacts with a transcritical temperature ramp at constant pressure. In this problem both the conservative and primitive branches of the method are active simultaneously, and the region flagged for conservative updating moves as the shock traverses the ramp.

The computation domain is $x \in [0, 1]$ m, discretized with $N_x = 500$ uniform cells and transmissive boundary conditions, as in the previous one-dimensional tests. At $t = 0$ a stationary Riemann problem is initialized at $x = x_s$, separating a uniform high-pressure left state and an inhomogeneous right state:

$$(\rho, u, p)(x, 0) = \begin{cases} (\rho_L, u_L, p_L), & x < x_s, \\ (\rho_R(x), u_R, p_R), & x > x_s, \end{cases} \tag{50}$$

where $p_L > p_R$ is chosen so that the resulting right-running shock has an upstream Mach number of order $M \simeq 1.5$ when measured in the nearly uniform region immediately to the right of the discontinuity. The right state represents a transcritical pseudo-boiling layer at constant pressure p_R, with prescribed temperature ramp

$$T(x, 0) = T_{\min} + \frac{T_{\max} - T_{\min}}{2} \left[1 - \tanh\left(\frac{x - x_0}{\eta} \right) \right], \tag{51}$$

where $T_{\min} < T_c < T_{\max}$ bracket the critical temperature of nitrogen and η controls the thickness of the ramp. The density field $\rho_R(x)$ is obtained from the real-gas EoS by solving $p(T, \rho) = p_R$ at each grid point, and the right state is initially at rest $u_R = 0$. This setup produces a right-moving shock that interacts with a spatially extended pseudo-boiling zone under nearly constant pressure.

Fig. 8 shows the numerical solution at $t = 1.8 \times 10^{-3}$ s for density, velocity, pressure, and temperature. The dashed curves in this figure corresponding to the initial condition and are plotted only as a reference, since no closed-form analytical solution is available for this real-gas, spatially inhomogeneous Riemann problem. The DOHD-WENO solution captures the leading right-running shock within a few grid cells. Downstream of the shock, the pressure remains nearly uniform across the pseudo-boiling region, despite the large variations in density and temperature imposed by the isobaric ramp. The temperature jump is resolved without spurious

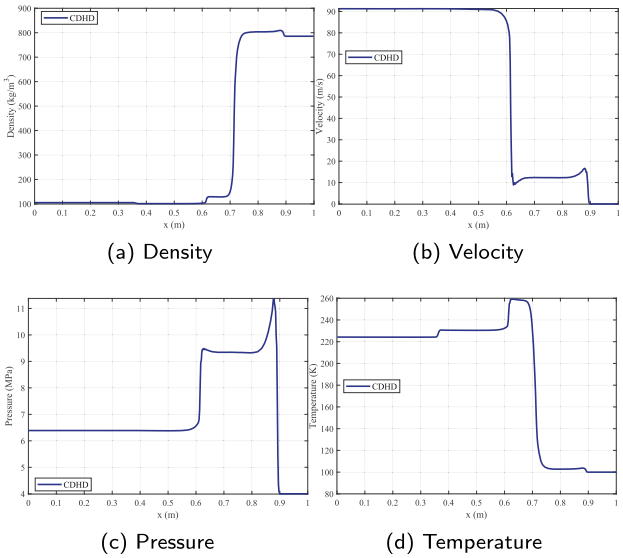

Fig. 8. Numerical solution of the one-dimensional shock–temperature-ramp interaction in transcritical nitrogen at $t = 1.8 \times 10^{-3}$ s. Profiles of (a) density, (b) velocity, (c) pressure, and (d) temperature are shown. The dashed curves indicate the initial condition used as a reference, while the CDHD–WENO solution captures the leading right-running shock within a few grid cells and maintains a nearly uniform pressure across the pseudo-boiling region despite large variations in density and temperature.

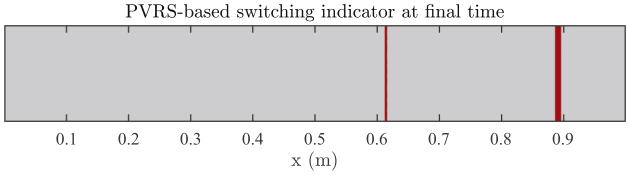

Fig. 9. PVRS-based switching indicator for the shock–temperature-ramp interaction at the same time as Fig. 8.Red cells are updated with the conservative WENO-Roe scheme, gray cells with the primitive CDHD scheme. The sensor is active only in narrow bands surrounding the propagating shock and its reflected/secondary waves.

oscillations in either pressure or velocity, illustrating that the primitive update remains well behaved in smooth transcritical regions even when a shock is present elsewhere in the domain.

The behavior of the switching mechanism is illustrated in Fig. 9, which plots the PVRS sensor at the same time instant. Cells flagged for conservative updating are shown with value 1, while cells updated in primitive form have value 0. The sensor is active only in narrow bands surrounding the propagating shock and its reflected/second waves. It remains essentially zero throughout the smooth pseudo-boiling layer. As the shock moves through the temperature ramp, the flagged region translates with the compression front and briefly enlarges when weak reflected waves are generated, but the bulk of the transcritical ramp is always advanced in primitive scheme. This example therefore provides a clean demonstration of the hybrid strategy: the conservative branch is activated automatically where sharp compressive features are present, while the primitive formulation is used elsewhere to preserve pressure equilibrium properties in the transcritical flow.

The structure of the resulting wave system can be understood in terms of the spatially varying thermodynamic properties along the ramp. As the shock enters the colder, denser portion of the pseudo-boiling layer, the local speed of sound increase with decreasing temperature at fixed pressure. The ramp therefore acts as a smoothly varying impedance transition. The incident compression is partly transmitted into the high impedance region and partly reflected upstream, producing small secondary waves that are visible in the velocity and pressure profiles. Because the sound speed is higher in the colder part of the ramp, trailing compression waves travel faster than the leading ones, gradually catching up and accumulating near the front. This wave accumulation leads to a local pressure overshoot relative to the nominal Rankine-Hugoniot jump, a characteristic feature of shock interactions with transcritical ramp. The PVRS mask aligns precisely with these localized compressive structures, activating the conservative update only where the wave steepening and reflection are strongest.

5.4. 2-D transcritical advection cases

To demonstrate the capability of the proposed scheme in multi-dimensional transcritical flows, we consider a 2D droplet convection problem that extends the 1D analysis to more realistic geometries. This test case examines the transport of a subcritical droplet through a supercritical environment under uniform advection.

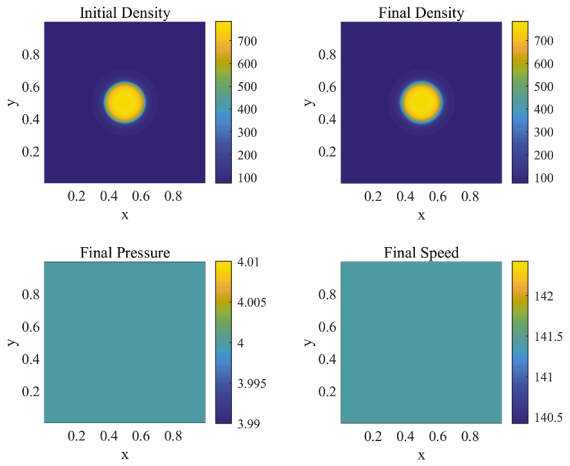

Fig. 10. Results for the 2D transcritical droplet advection case at the final time of $t = 0.01$ s (one period). The figure displays the initial and final density fields, along with the final pressure and speed. The droplet maintains its circular shape with minimal numerical diffusion, while the pressure and speed fields remain uniform, demonstrating the accuracy of the proposed scheme.

The computational domain is defined as $\Omega \in [0,1] \times [0,1]$ m with a uniform Cartesian grid of 151×151 cells. The initial state is a circular droplet centered at $(x_c, y_c) = (0.5, 0.5)$ m with radius $r_d = 0.15$ m. The temperature field is initialized using a smooth hyperbolic tangent profile to represent the droplet interface:

$$T(x,y) = T_{\text{ambient}} \tag{52}$$

$$+ (T_{\text{droplet}} - T_{\text{ambient}}) \cdot \frac{1}{2}\left[1 - \tanh\left(\frac{r - r_d}{\eta}\right)\right], \tag{53}$$

where $r = \sqrt{(x - x_c)^2 + (y - y_c)^2}$ is the radial distance from the droplet center, $T_{\text{droplet}} = 100$ K represents the subcritical liquid phase, $T_{\text{ambient}} = 200$ K corresponds to the supercritical gas phase, and $\eta = 0.05$ controls the interface thickness. The velocity and pressure fields are initialized as spatially uniform:

$$\mathbf{u}(x,y) = (100, 100)^T \text{ m/s}, \quad p(x,y) = 4.0 \times 10^6 \text{ Pa}. \tag{54}$$

The density field $\rho(x,y)$ is computed from the temperature and pressure using the PR EoS. The simulation runs until $t = 0.01$s with CFL $= 0.5$, corresponding to one complete convection time. This set up allows the initial state to serve as a analytical solution.

Fig. 10 presents the evolution of the transcritical droplet convection, showing the initial and final density distributions along with the final pressure and velocity magnitude fields. The density field evolution reveals that the droplet maintains its circular shape and sharp interface throughout the convection process. The initial density contrast between the subcritical droplet core and the supercritical ambient medium is preserved without significant numerical diffusion. The absence of spurious oscillations near the steep density gradients confirms the efficacy of the WENO-5 reconstruction in handling transcritical interfaces. The pressure and velocity fields exhibit uniformity across the entire domain. The proposed scheme successfully maintains pressure equilibrium while resolving the dramatic thermodynamic variations at the droplet interface. These results confirm that the high-order primitive update with small characteristic-based dissipation transports sharp real-gas gradients cleanly while preserving the constant velocity and pressure fields.

5.5. 2D shock-droplet advection

A weak oblique shock crosses a translating, transcritical droplet (the 2-D advection case in §5.3 is extended). Again, the mask shows switching near the shock and primitive updates elsewhere.

To assess the hybrid scheme in a genuinely two-dimensional setting we extend the transcritical droplet advection problem by adding a weak oblique shock. The computational domain is $[0,1] \times [0,1]$ discretized on uniform 151×151 grid, with the same real-gas EoS as in the previous testes.

A circular droplet of radius $r_d = 0.15$ is initially centered at $(x_c, y_c) = (0.25, 0.5)$ and smoothed with a hyperbolic tangent profile of thickness $\eta = 0.05$. The temperature field is prescribed as isobaric ramp:

$$T(x,y) = T_\infty(x,y) + \left(T_d - T_\infty(x,y)\right) \frac{1}{2}\left[1 - \tanh\left(\frac{r - r_d}{\eta}\right)\right], \tag{55}$$

where $r = \sqrt{(x - x_c)^2 + (y - y_c)^2}$, $T_d = 100$ K is the droplet temperature and $T_\infty = 200$ K is the ambient temperature. The pressure is initially uniform upstream at $p_1 = 4$ MPa and the local ambient velocity is a uniform vector aligned with the normal to the shock, so that the droplet is in both pressure and velocity equilibrium with its surroundings.

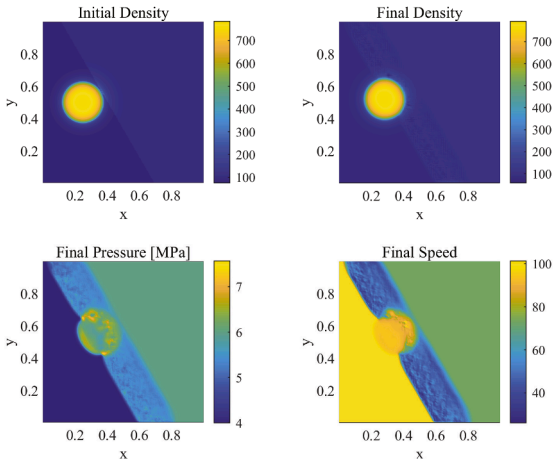

Fig. 11. Results for the two-dimensional shock–droplet advection case at $t = 0.3\,t_{\text{cross}}$. The panels show the initial density field and the density, pressure, and speed magnitude at $t = 0.3\,t_{\text{cross}}$ for a weak oblique shock interacting with a translating transcritical droplet. The strongest gradients are confined to a thin region enveloping the shock and the droplet interface, while the bulk of the domain remains smooth and close to pressure equilibrium, illustrating the robustness of the hybrid CDHD–WENO scheme.

Table 2
Wall-clock CPU time for the 1D advection test ($N_x = 512$, $t_{\text{final}} = 0.01$ s). T_{CDHD}, T_{hyb}, and T_{Roe} denote the primitive-only, hybrid, and fully conservative schemes, respectively.

Scheme	N_x	T [s]	Steps	T/T_{CDHD}
Primitive-only CDHD	512	31.34	3529	1.00
Hybrid CDHD + Roe	512	117.63	3529	3.75
Conservative Roe	512	78.63	3519	2.51

A weak planar shock with normal Mach number $M \approx 1.2$ is imposed by prescribing upstream and downstream states. The shock normal is oriented at $\theta = 30°$ with respect to the x -axis, so that the planar front intersects the domain diagonally. The shock plane is given by $\mathbf{n} \cdot \mathbf{x} = s_0$, where $\mathbf{n} = (\cos\theta, \sin\theta)$ is the unit normal. For $n \cdot x < s_0$ the flow is in the upstream state $(\rho_1, T_1, p_1, \boldsymbol{u}_1)$, and for $\mathbf{n} \cdot \mathbf{x} > s_0$ we prescribe the downstream state $(\rho_2, T_2, p_2, \boldsymbol{u}_2)$ obtained from weak-shock jump relations using an effective ratio of specific heats $\gamma_{\text{eff}} = 1.3$. The velocity is everywhere aligned with $\mathbf{n}$, so that the droplet is exactly advected by the local ambient flow. The solution is advanced to $t = 0.3\,t_{\text{cross}}$, where t_{cross} is the time for the droplet center to reach the undisturbed shock plane.

Fig. 11 summarizes the evolution. The initial density field shows the isobaric droplet embedded in the piecewise constant ambient separated by the oblique shock. At $t = 0.3\,t_{\text{cross}}$ the shock has intersected the droplet and generated a curved transmitted wave and a weak reflected disturbance. The final pressure and speed panels reveal that the strongest gradients are confined to a thin region enveloping the shock and the droplet interface, while the bulk of the domain remains smooth and close to pressure equilibrium.

5.6. Computational cost

The hybrid CDHD strategy couples a primitive-variable update with a conservative WENO–Roe scheme. Given the dual nature of the algorithm, it is necessary to assess the computational cost relative to standard single-branch solvers.

We utilize the one-dimensional advection case described in Section 5.1 with $N_x = 512$. To allow for a direct comparison, we employ a relaxed initial condition ($\eta = 0.2$, $p_0 = 8$ MPa) that ensures stability for the standard conservative Roe solver, which otherwise fails on stiffer transcritical cases. Time integration is performed via a third-order TVD Runge–Kutta method (CFL= 0.8) until $t_{\text{final}} = 0.01$ s. Three solver configurations are evaluated:

1. **Primitive-only CDHD**: Uses the proposed primitive-variable flux globally.
2. **Hybrid CDHD + Roe**: Uses the PVRS sensor to switch between CDHD and conservative WENO–Roe fluxes.
3. **Conservative Roe**: Uses the real-gas Roe flux globally with WENO-5 reconstruction.

Simulations were conducted using a serial MATLAB implementation on an *AMD Ryzen 9 7945HX* processor. Table 2 summarizes the wall-clock time T and the relative cost T/T_{CDHD}.

The results demonstrate that the primitive-only CDHD method is the most efficient, as it avoids the computationally expensive eigen-decomposition required by the Roe solver. The fully conservative scheme is approximately 2.5× more expensive than the primitive formulation. The current hybrid implementation exhibits the highest cost (3.75×); however, this is an artifact of the unoptimized

prototype code, which computes *both* the primitive and conservative fluxes for every cell at every sub-step before applying the switching mask.

Despite the higher computational cost, the hybrid scheme offers essential robustness. In the sharper transcritical configuration ($p_0 = 4$ MPa, $\eta = 0.1$), the standard fully conservative Roe solver fails to complete the simulation, whereas the hybrid method remains stable. In a production environment (e.g., using conditional branching in C++ or Fortran), the hybrid cost would be significantly reduced by evaluating the Roe flux only in flagged cells. Consequently, the reported cost ratio of 3.75 should be interpreted as a pessimistic upper bound.

6. Conclusion

We proposed the Central Differential flux with High-Order Dissipation (CDHD) to address spurious oscillations and energy conservation errors in transcritical flow simulations. The method combines a central flux with minimal upwind-biased dissipation, achieving second-order accuracy in smooth regions while substantially improving energy conservation. Embedded in a hybrid framework with a conservative shock-capturing scheme, CDHD demonstrates robust performance across both smooth and shock-containing flows. These results establish CDHD as a reliable and efficient approach for real-gas simulations in engineering and scientific applications.

Declaration of generative AI and AI-assisted technologies in the writing process

During the preparation of this work the authors used ChatGPT and Gemini in order to improve readability and language of the work. After using this tool/service, the author(s) reviewed and edited the content as needed and take(s) full responsibility for the content of the publication.

CRediT authorship contribution statement

Bonan Xu: Writing – original draft, Writing – review & editing, Methodology, Investigation, Conceptualization, Formal analysis, Validation; **Chang Sun:** Writing – original draft, Investigation, Formal analysis; **Peixu Guo:** Writing – review & editing, Validation, Supervision, Project administration, Investigation, Funding acquisition.

Data availability

Data will be made available on request.

Declaration of competing interest

The authors declare that they have no known competing financial interests or personal relationships that could have appeared to influence the work reported in this paper.

Acknowledgement

This work is supported by the Hong Kong Research Grants Council (GRF no.15203724) and the Start-up Fund for RAPs by the Hong Kong Polytechnic University.

Appendix A.

Following previous work on the Peng-Robinson (PR) equation of state (EoS), this appendix gives more details about the conversions we use when alternating between the conservative total energy update(Section 3.4) and the primitive/pressure update (Section 3.5), and it lists the thermodynamic closures needed to reproduce our results. The PR EoS used in this work is given in Eq. 4 with parameter a, b from Eq. 7. The internal energy relation and speed of sound in Eq. 8.

A.1. The derivatives of PR EoS for closure

The PR EoS in mass specific variables can be written as:

$$P = \frac{\rho R_u T}{M_w - b\rho} + \frac{a\alpha(T)\rho^2}{M_w^2 + 2M_w b\rho - b^2\rho^2}. \tag{A.1}$$

Then the first and second derivatives used blow are:

$$\begin{aligned}\left(\frac{\partial p}{\partial \rho}\right)_T &= \frac{R_u T M_w}{D_1^2} \\ &\quad - \frac{\left(2a\alpha_{\mathrm{PR}}\rho\right)D_2 - a\alpha_{\mathrm{PR}}\rho^2\left(2M_w b - 2b^2\rho\right)}{D_2^2}, \\ \left(\frac{\partial p}{\partial T}\right)_\rho &= \frac{\rho R_u}{D_1} + \frac{a\rho^2\alpha'_{\mathrm{PR}}(T)}{D_2}, \\ \left(\frac{\partial^2 p}{\partial T^2}\right)_\rho &= \frac{a\rho^2\alpha''_{\mathrm{PR}}(T)}{D_2}.\end{aligned} \tag{A.2}$$

The temperature derivatives of $\alpha(T)$ for Peng-Robinson EoS are:

$$\alpha'(T) = -\frac{m\phi(T)}{T_c\sqrt{T/T_c}}, \quad \alpha''(T) = \frac{m(1+m)}{2T_c^2\left(\sqrt{T/T_c}\right)^3}, \tag{A.3}$$

with $\phi(T) = 1 + m\left(1 - \sqrt{T/T_c}\right)$.

A.2. Heat capacities and speed of sound

From Eq. 4 and the above derivatives, the constant volume heat capacity $c_v(T,\rho)$ is:

$$\begin{aligned}c_v(T,\rho) &= \left(\frac{\partial e}{\partial T}\right)_\rho = c_{v,0}(T) - T\int_{\rho_0}^{\rho}\frac{1}{\rho'^2}\left(\frac{\partial^2 p}{\partial T^2}\right)_{\rho'}\mathrm{d}\rho', \\ c_{v,0}(T) &= c_{p,0}(T) - R_s.\end{aligned} \tag{A.4}$$

Here the $c_{v,0}$ and $c_{p,0}$ represent the constant volume and constant pressure heat capacities of ideal gas.

The constant pressure heat capacity is then obtained from the standard identity:

$$c_p(T,\rho) = c_v(T,\rho) + \frac{T}{\rho^2}\frac{\left[\left(\frac{\partial p}{\partial T}\right)_\rho\right]^2}{\left(\frac{\partial p}{\partial \rho}\right)_T}. \tag{A.5}$$

Finally, the speed of sound used by the primitive update and by the PVRS sensor is evaluated as

$$c^2 = \left(\frac{\partial p}{\partial \rho}\right)_s = \frac{c_p}{c_v}\left(\frac{\partial p}{\partial \rho}\right)_T, \tag{A.6}$$

with c_p/c_v and $(\partial p/\partial\rho)_T$ from the above formulas.

A.3. Conversion relations between pressure and internal energy

The method developed in this paper alternates between solving the total-energy and pressure equations. This section will provide the detail conversion relations between pressure and internal energy.

In the conservative step, given the updated (ρ, u, E) we compute

$$e = \frac{E}{\rho} - \frac{u^2}{2}. \tag{A.7}$$

We then solve for T at fixed ρ from $g(T) = e(T,\rho) - e = 0$ using Newton iterations:

$$T^{(k+1)} = T^{(k)} - \frac{e\left(T^{(k)},\rho\right) - e}{c_v\left(T^{(k)},\rho\right)}, \tag{A.8}$$

with initial guess $T^{(0)}$ from the previous time step and stopping when $|\Delta T|/T < 10^{-10}$. Pressure is then $p = p(\rho,T)$ from Eq. 4.

Given (ρ, u, p) updated in the primitive step, we can recover T at fixed ρ from $f(T) = p(\rho,T) - p = 0$ by Newton iterations:

$$T^{(k+1)} = T^{(k)} - \frac{p\left(\rho,T^{(k)}\right) - p}{\left(\frac{\partial p}{\partial T}\right)_\rho\left(T^{(k)}\right)}. \tag{A.9}$$

Wen then evaluate $e = e(T,\rho)$ and update:

$$E = \rho e + \frac{1}{2}\rho u^2. \tag{A.10}$$

Supplementary material

Supplementary material associated with this article can be found, in the online version, at 10.1016/j.jcp.2026.114653.

References

[1] A. Guardone, P. Colonna, M. Pini, A. Spinelli, Nonideal compressible fluid dynamics of dense vapors and supercritical fluids, Annu. Rev. Fluid Mech. 56 (2024) 241–269.
[2] J. Manin, M. Bardi, L.M. Pickett, R.N. Dahms, J.C. Oefelein, Microscopic investigation of the atomization and mixing processes of diesel sprays injected into high pressure and temperature environments, Fuel 134 (2014) 531–543.
[3] G. Singla, P. Scouflaire, C. Rolon, S. Candel, Transcritical oxygen/transcritical or supercritical methane combustion, Proc. Combust. Inst. 30 (2005) 2921–2928.
[4] R. Votta, F. Battista, V. Salvatore, M. Pizzarelli, G. Leccese, F. Nasuti, S. Meyer, Experimental investigation of transcritical methane flow in rocket engine cooling channel, Appl. Therm. Eng. 101 (2016) 61–70.
[5] B. Chehroudi, Recent experimental efforts on high-pressure supercritical injection for liquid rockets and their implications, 1, 2012, p. 121802.
[6] Y.M. Kim, C.G. Kim, D. Favrat, Transcritical or supercritical CO2 cycles using both low- and high-temperature heat sources, 2nd International Meeting on Cleaner Combustion (CM0901-Detailed Chemical Models for Cleaner Combustion) 43 (2012) 402–415.
[7] L. Qin, G. Xie, Y. Ma, S. Li, Thermodynamic analysis and multi-objective optimization of a waste heat recovery system with a combined supercritical/transcritical CO2 cycle, Energy 265 (2023) 126332.
[8] C. Zhu, Y. Zhang, M. Wang, J. Deng, Y. Cai, W. Wei, M. Guo, Simulation and comprehensive study of a new trigeneration process combined with a gas turbine cycle, involving transcritical and supercritical CO2 power cycles and goswami cycle, J. Therm. Anal. Calorim. 149 (12) (2024) 6361–6384.
[9] C. Leng, X.-D. Wang, W.-M. Yan, T.-H. Wang, Heat transfer enhancement of microchannel heat sink using transcritical carbon dioxide as the coolant, Energy Convers. Manage. 110 (2016) 154–164.
[10] P. Zhang, D.-W. Wang, W.-S. Zhao, Investigation on embedded microchannel heatsink for 2.5-d integrated package, IEEE Trans. Compon. Packag. Manuf. Technol. 13 (6) (2023) 838–848.
[11] J. Luo, L. Xu, E. Lascaris, H.E. Stanley, S.V. Buldyrev, Behavior of the widom line in critical phenomena, Phys. Rev. Lett. 112 (2014) 135701.
[12] D. Gallo, M. Corradini, Rovere, Widom line and dynamical crossovers as routes to understand supercritical water, Nat. Commun. 5 (1) (2014) 5806.
[13] J. Ren, M. Kloker, Instabilities in three-dimensional boundary-layer flows with a highly non-ideal fluid, J. Fluid Mech. 951 (9) (2022) A9.
[14] J. Poblador-Ibanez, W.A. Sirignano, F. Hussain, Vorticity dynamics in transcritical liquid jet breakup, J. Fluid Mech. 978 (6) (2024) A6.
[15] F. Li, W. Zhang, B. Bai, M. Ihme, Small-scale turbulent characteristics in transcritical wall-bounded flows, J. Fluid Mech. 986 (2024) A36.
[16] J. Ren, Y. Wu, X. Mao, C. Wang, M. Kloker, Sensitivity of three-dimensional boundary layer stability to intrinsic uncertainties of fluid properties: a study on supercritical CO2, J. Fluid Mech. 1007 1007:A7, 2025.
[17] M. Bernades, F. Capuano, L. ś Jofre, Microconfined high-pressure transcritical fluid turbulence, Phys. Fluids 35 (1) 2023.
[18] C. Peter, Y. Ma, M. Lv, Ihme, An entropy-stable hybrid scheme for simulations of transcritical real-fluid flows, J. Comput. Phys. 340 (2017) 330–357.
[19] V.A. Dobrev, T.V. Kolev, R.N. Rieben, V.Z. Tomov, Multi-material closure model for high-order finite element lagrangian hydrodynamics, Int. J. Numer. Methods Fluids 82 (10) (2016) 689–706.
[20] E.J. Ching, R.F. Johnson, A.D. Kercher, Conservative, pressure-equilibrium-preserving discontinuous galerkin method for compressible, Technical Report, multicomponent flows. arXiv preprint, 2025.
[21] R.W. Houim, K.K. Kuo, A low-dissipation and time-accurate method for compressible multi-component flow with variable specific heat ratios, J. Comput. Phys. 230 (23) (2011) 8527–8553.
[22] Y. Lv, M. Ihme, Discontinuous Galerkin method for multicomponent chemically reacting flows and combustion, J. Comput. Phys. 270 (2014) 105–137.
[23] D.-Y. Peng, D.B. Robinson, A new two-constant equation of state, Ind. Eng. Chem. Fundam. 15 (1) (1976) 59–64.
[24] J.M. B.E. Poling, O. Prausnitz, J. Connell, R.C. Paul, Reid, The properties of gases and liquids, 5, Mcgraw-hill, New York, New York, 2001.
[25] P.E. Lapenna, R. Lamioni, P.P. Ciottoli, F. Creta, Low-Mach number simulations of transcritical flows.
[26] P. Eduardo, Lapenna, F. Creta, Mixing under transcritical conditions: an a-priori study using direct numerical simulation, J. Supercrit. Fluids 128 (2017) 263–278.
[27] F. Battista, F. Picano, C.M. Casciola, Turbulent mixing of a slightly supercritical van der waals fluid at low-mach number, Phys. Fluids 26 (5) (2014).
[28] P. Eduardo, Lapenna, Characterization of pseudo-boiling in a transcritical nitrogen jet, Phys. Fluids 30 (PLXPAGE07 2018) 77106.
[29] R. Abgrall, S. Karni, Computations of compressible multifluids, J. Comput. Phys. 169 (2) (2001) 594–623.
[30] S. Yatsuyanagi, T. Furusawa, S. Yamamoto, Double-flux model for supercritical multicomponent flows at low mach numbers with preconditioning method, J. Comput. Phys. 458 (2022) 111091.
[31] C. Rodriguez, A. Vidal, P. Koukouvinis, M. Gavaises, M.A. Mchugh, Simulation of transcritical fluid jets using the pc-saft eos, J. Comput. Phys. 374 (2018) 444–468.
[32] A. Peyvan, D. Li, J. Komperda, F. Mashayek, Oscillation-free nodal discontinuous spectral element method for the simulation of compressible multicomponent flows, J. Comput. Phys. 452 (2022) 110921.
[33] S. Karni, Viscous shock profiles and primitive formulations, SIAM J. Numer. Anal. 29 (6) (1992) 1592–1609.
[34] S. Karni, Multicomponent flow calculations by a consistent primitive algorithm, J. Comput. Phys. 112 (1) (1994) 31–43.
[35] H. Terashima, M. Koshi, Approach for simulating gas-liquid-like flows under supercritical pressures using a high-order central differencing scheme, J. Comput. Phys. 231 (20) (2012) 6907–6923.
[36] S. Kawai, H. Terashima, H. Negishi, A robust and accurate numerical method for transcritical turbulent flows at supercritical pressure with an arbitrary equation of state, J. Comput. Phys. 300 (2015) 116–135.
[37] S. Karni, Hybrid multifluid algorithms, SIAM J. Sci. Comput. 17 (5) (1996) 1019–1039.
[38] R. Fedkiw, X.-D. Liu, S. Osher, A general technique for eliminating spurious oscillations in conservative schemes for multiphase and multispecies euler equations, Int. J. Nonlinear Sci. Numer. Simul. 3 (2) (2002) 99–106.
[39] B. Boyd, D. Jarrahbashi, A diffuse-interface method for reducing spurious pressure oscillations in multicomponent transcritical flow simulations, Comput. Fluids 222 (2021) 104924.
[40] E.J. Ching, R.F. Johnson, A.D. Kercher, Conservative, Pressure-Equilibrium-Preserving Discontinuous Galerkin method for Compressible, 2025. Multicomponent flows.
[41] E.J. Ching, R.F. Johnson, A.D. Kercher, A note on Reducing Spurious Pressure Oscillations in Fully Conservative Discontinuous Galerkin Simulations of Multicomponent Flows, 2023.
[42] R.F. Johnson, A.D. Kercher, A conservative discontinuous galerkin discretization for the chemically reacting navier-stokes equations, J. Comput. Phys. 423 (2020) 109826.
[43] N. Franchina, M. Savini, F. Bassi, Multicomponent gas flow computations by a discontinuous Galerkin scheme using l2-projection of perfect gas eos, J. Comput. Phys. 315 (2016) 302–322.
[44] S.C. Spiegel, J.R. Huynh, Debonis, De-Aliasing through Over-Integration Applied to the Flux Reconstruction and Discontinuous Galerkin Methods.
[45] Y. Fujiwara, Y. Tamaki, S. Kawai, Fully conservative and pressure-equilibrium preserving scheme for compressible multi-component flows, J. Comput. Phys. 478 (2023) 111973.
[46] H. Terashima, N. Ly, M. Ihme, Approximately pressure-equilibrium-preserving scheme for fully conservative simulations of compressible multi-species and real-fluid interfacial flows, J. Comput. Phys. 524 (2025) 113701.

[47] M. Bernades, L. Jofre, F. Capuano, Kinetic-energy- and pressure-equilibrium-preserving schemes for real-gas turbulence in the transcritical regime, J. Comput. Phys. 493 (2023) 112477.
[48] C. Pietro, R. Boldini, P. Hirai, Costa, W.R. Jurriaan, R. Peeters, Pecnik, CUBENS: a gpu-accelerated high-order solver for wall-bounded flows with non-ideal fluids, Comput. Phys. Commun. 309 (2025) 109507.
[49] F. Eleuterio, Toro, Riemann Solvers and Numerical Methods for Fluid Dynamics: A Practical Introduction, Springer Science & Business Media, 2013.
[50] G.-S. Jiang, C.-W. Shu, Efficient implementation of weighted eno schemes, J. Comput. Phys. 126 (1) (1996) 202–228.
[51] S. Arabi, J.-Y. Trépanier, R. Camarero, A simple extension of roe's scheme for real gases, J. Comput. Phys. 329 (2017) 16–28.
[52] S.-K. Kim, H.-S. Choi, Y. Kim, Thermodynamic modeling based on a generalized cubic equation of state for kerosene/lox rocket combustion, Combust. Flame. 159 (3) (2012) 1351–1365.
[53] J.S. Hesthaven, Numerical methods for conservation laws: from analysis to algorithms, 2017.
[54] B.J. Lee, E.F. Toro, C.E. Castro, N. Nikiforakis, Adaptive osher-type scheme for the Euler equations with highly nonlinear equations of state, J. Comput. Phys. 246 (2013) 165–183.
[55] M. Dumbser, F. Eleuterio, Toro, A simple extension of the osher riemann solver to non-conservative hyperbolic systems, J. Sci. Comput. 48 (1) (2011) 70–88.